

Modelling Cross-polarisation Patterns of Axially-symmetrical Monopulse Antennas for Cross-polarisation Jamming Analysis

KHAHLISO MOSOMA 

University of Pretoria, Pretoria, South Africa
Council for Scientific and Industrial Research (CSIR),
Pretoria, South Africa

WARREN P. DU PLESSIS , Senior Member, IEEE
University of Pretoria, Pretoria, South Africa

Abstract—Most radar systems do not consider the situation where the return is dominated by the polarisation orthogonal to the polarisation transmitted by the radar. A cross-polarisation jammer exploits this limitation by transmitting a signal with this orthogonal polarisation to cause an angular error. Mathematical models of cross-polarisation monopulse patterns are derived, and their results are shown to be similar to those of five simulated monopulse antennas and one measured monopulse antenna. The polarisation accuracy of the jammer is shown to play a crucial role, with the jammer needing high polarisation accuracy. The induced angular error increases slowly when the jammer-to-signal ratio (JSR) is between

Manuscript received 30 Jul. 2024; revised 29 Nov. 2024; accepted to be determined (TBD). Date of publication TBD; date of current version 29 Nov. 2024.

DOI: ??./TAES.???.?????

Refereeing of this contribution was handled by A. N. Editor.

Khahliso Mosoma is with the Department of Electrical, Electronic and Computer Engineering, University of Pretoria, Pretoria, 0002, South Africa and the Council for Scientific and Industrial Research (CSIR), Pretoria, 0001, South Africa (e-mail: kmosoma@csir.co.za). Warren P. du Plessis is with the Department of Electrical, Electronic and Computer Engineering, University of Pretoria, Pretoria, 0002, South Africa (e-mail: wduplessis@ieee.org).
(Corresponding author: Khahliso Mosoma.)

0018-9251 © 2024 IEEE

0 dB and 20 dB and increases faster when the JSR is greater than 20 dB.

Index Terms—Cross-polarisation jamming, electronic countermeasures (ECM), radar tracking, radar antennas, and electronic warfare (EW).

I. INTRODUCTION

Cross-polarisation jamming is an electronic attack (EA), or electronic countermeasures (ECM), technique that can induce angular errors in radars [1]. Most radar systems only use one polarisation, which is called the co-polarisation component, with the component of the radar transmission that is orthogonal to the co-polarisation being called the cross-polarisation component [1], [2], [3]. A cross-polarisation jammer seeks to cause a large cross-polarisation component to be received by a radar, thereby causing an angular tracking error [2], [3], [4].

This angular tracking error arises because the tracking behaviour of most radars differs for the co- and cross-polarisation components of the received signal [5], [6], [7]. This weakness is seen in the cross-polarisation sum components of a monopulse radar having nulls on the azimuth and elevation axes and peaks called Condon lobes in the $\pm 45^\circ$ diagonal planes [2], [8], [9], [10]. The nulls are caused by the cancellation of the cross-polarisation component which results from the symmetry of the antennas in each quadrant [11]. In parabolic reflectors, these Condon lobes are influenced by the focal-length-to-diameter (F/D) ratio of the reflector, with the Condon lobes decreasing as the F/D ratio increases [8], [9], [10].

In most radars, the co-polarisation component is on the order of 20 dB greater than the cross-polarisation component [12]. To counteract this, the jammer must be able to determine the polarisation of a received signal with high accuracy and to re-transmit the signal with a precisely-controlled polarisation to ensure a polarisation accuracy of around 5° relative to the received signal [4], [5], [12]. Additionally, the jammer polarisation purity must be greater than the radar polarisation purity for successful cross-polarisation jamming [6]. Ultimately, this means that a cross-polarisation jammer must have a jammer-to-signal ratio (JSR) of between 20 and 40 dB to induce a significant angular error in a tracking radar [5], [12]. Importantly, a cross-polarisation jammer will act as a beacon and assist the radar in tracking the target if the cross-polarisation component of the jamming signal does not exceed its co-polarisation component at the radar by a sufficiently large margin [1], [13].

To theoretically analyse cross-polarisation jamming, it is necessary to use co- and cross-polarisation antenna

pattern models. Even though there is information about the cross-polarisation patterns of monopulse antennas (e.g. [12]), there is no effective mathematical model of the cross-polarisation pattern [14]. Gaussian functions can be used to represent the antenna patterns and co-polarisation patterns [13], or monopulse antenna patterns can be modelled using trigonometric functions and element patterns [15], but again the cross-polarisation component is not considered.

The majority of analyses of cross-polarisation jamming are limited to considering simulations of specific antennas rather than generally-applicable analyses of the underlying effects [14], [16]. Cross-polarisation jamming has been analysed mathematically [13], [14], [17], but constraints including limited consideration of antenna patterns and the use of fixed random numbers to represent the phase pattern of the cross-polarisation component limit the applicability of these analyses. This limited published modelling of cross-polarisation jamming means that the origin of guidelines such as the JSR and polarisation accuracy noted above is unclear.

In an attempt to address this limitation, mathematical modelling of cross-polarisation jamming is presented. This analysis focuses on the diagonal planes as these planes contain the peaks of the Condon lobes. The derived models generate the co- and cross-polarisation antenna patterns, monopulse ratios, and polarisation purity for both the sum and difference patterns as this information is required for a comprehensive analysis of cross-polarisation jamming.

Five monopulse antennas with a variety of different characteristics, including amplitude- and phase-comparison monopulse with a range of implementations, including reflector antennas, planar array antennas, and horn antennas, are evaluated. Furthermore, one of these antennas was manufactured and measured to validate the simulated results. In this way, the limited applicability of previous works is addressed.

The primary outcome of this work is that the validity of the widely-quoted JSR and polarisation-purity requirements are studied. This analysis shows that the cross-polarisation jamming may have more potential in jamming monopulse radars than the literature suggests, but that the polarisation accuracy required is more stringent than widely believed.

II. CO- AND CROSS-POLARISATION PATTERN MODELLING

Two techniques are presented to model the co- and cross-polarisation radiation patterns of a monopulse antenna. The difference between the techniques is that

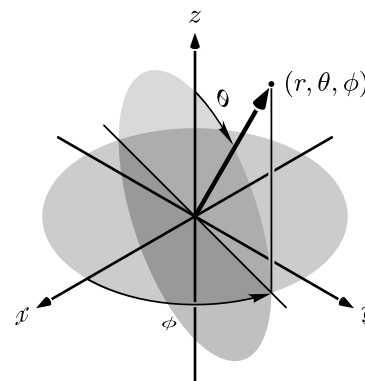


Fig. 1. The co-ordinate system showing the relationship between the spherical (r, ϕ, θ) and Cartesian co-ordinates (x, y, z) used in this work.

Technique 1 in Section II-A uses Ludwig's third polarisation definition [18] to split the array pattern into co- and cross-polarisation patterns, while Technique 2 in Section II-B uses a different technique to split the array pattern into co- and cross-polarisation patterns. These techniques use linear polarisation. While the focus is on cross-polarisation patterns, the co-polarisation patterns are also modelled in each technique as the relationship between the polarisations plays a significant role in cross-polarisation jamming.

The analysis is for cross-polarisation jamming, so the main focus is on the Condon lobes located precisely in the diagonal planes of the antennas in this work. Due to the symmetry of the Condon lobes, only the diagonal plane at 45° to the horizontal is analysed in the derived models.

The spherical co-ordinate system used in this work is shown in Fig. 1, with ϕ measured in the x - y plane from the x axis towards the y axis, and θ measured from the positive z axis. The antenna is positioned in the x - y plane ($z = 0$), so that its boresight direction is in the \hat{z} direction where $\theta = 0^\circ$. This configuration is used because it means that θ corresponds to the angle from boresight, and ϕ corresponds to the polarisation angle.

The azimuth plane is the x - z plane where $y = 0$ with $\phi = 0^\circ$ and 180° , and the elevation plane is the y - z plane where $x = 0$ with $\phi = 90^\circ$ and 270° . The two diagonal planes have $x = y$ when $\phi = 45^\circ$ and 225° , and $x = -y$ when $\phi = 135^\circ$ and 315° . Two ϕ angles are required to indicate planes because $\theta \in [0^\circ, 180^\circ]$, but the remainder of this document will only indicate the smaller of the two ϕ values to keep the notation concise. The antennas considered will have vertical polarisation, so the co- and cross-polarised electric fields in the plane of the antenna, $z = 0$, are in the \hat{y} and $-\hat{x}$ directions, respectively.

Even though the analysis is performed in the diagonal planes, the derived models can be used to analyse other planes. Technique 1 in Section II-A can be used in the azimuth and elevation planes, while Technique 2 in Section II-B can be used in all the planes. These models are for axially-symmetrical phase and amplitude-comparison monopulse antennas.

The monopulse models used in this work to derive the cross-polarisation patterns apply to all types of monopulse antennas [15], [19].

A. Technique 1

The co- and cross-polarisation radiation patterns of an antenna in spherical co-ordinates are represented by [18], [20]

$$E_C(\theta, \phi) = \mathbf{E}(\theta, \phi) \cdot \hat{\mathbf{i}}_C \quad (1)$$

$$E_X(\theta, \phi) = \mathbf{E}(\theta, \phi) \cdot \hat{\mathbf{i}}_X, \quad (2)$$

respectively, with \cdot indicating the dot or scalar product, $\hat{\mathbf{i}}_C$ and $\hat{\mathbf{i}}_X$ being the linear co- and cross-polarisation unit vectors from Ludwig's third polarisation definition [18],

$$\hat{\mathbf{i}}_C = \sin(\phi) \hat{\boldsymbol{\theta}} + \cos(\phi) \hat{\boldsymbol{\phi}} \quad (3)$$

$$\hat{\mathbf{i}}_X = \cos(\phi) \hat{\boldsymbol{\theta}} - \sin(\phi) \hat{\boldsymbol{\phi}}, \quad (4)$$

and $\mathbf{E}(\theta, \phi)$ being the electric field with

$$\mathbf{E}(\theta, \phi) = E_\theta(\theta, \phi) \hat{\boldsymbol{\theta}} + E_\phi(\theta, \phi) \hat{\boldsymbol{\phi}}, \quad (5)$$

where $E_\theta(\theta, \phi)$ and $E_\phi(\theta, \phi)$ are the electric fields in the $\hat{\boldsymbol{\theta}}$ and $\hat{\boldsymbol{\phi}}$ directions, respectively.

Ludwig's third polarisation definition is used because it defines polarisations in spherical co-ordinates, which is how practical antennas radiate their radiation patterns [18]. The challenge is to model the $\mathbf{E}(\theta, \phi)$ patterns of a monopulse antenna that will give the expected polarisation components in the main planes (azimuth and elevation) and the diagonal planes.

In the analysed antennas, it is seen that $E_\theta(\theta, \phi_a) \approx 0$ in azimuth plane at $\phi_a = 0^\circ$ giving

$$\mathbf{E}(\theta, \phi_a) \approx E_\phi(\theta, \phi_a) \hat{\boldsymbol{\phi}}, \quad (6)$$

$E_\phi(\theta, \phi_e) \approx 0$ in the elevation plane with $\phi_e = 90^\circ$ giving

$$\mathbf{E}(\theta, \phi_e) \approx E_\theta(\theta, \phi_e) \hat{\boldsymbol{\theta}}, \quad (7)$$

and $E_\theta(\theta, \phi_d) \approx E_\phi(\theta, \phi_d) = E_d(\theta, \phi_d)$ in the diagonal planes $\phi_d = \pm 45^\circ$ giving

$$\mathbf{E}(\theta, \phi_d) \approx E_d(\theta, \phi_d) [\hat{\boldsymbol{\theta}} \pm \hat{\boldsymbol{\phi}}]. \quad (8)$$

The approximations above are required instead of equalities to avoid the cross-polarisation components calcu-

lated from Ludwig's third polarisation definition [18] becoming zero and preventing the modelling of cross-polarisation components including Condon lobes.

To model the sum-channel electric field in the azimuth direction, the array pattern from two antennas that are spaced at a distance of $\pm d/2$ from the origin, is given by [15]

$$\mathbf{E}_\Sigma(\theta, \phi_a) = \mathbf{P}_1(\theta, \phi_a) e^{j\psi(\theta, \phi_a)} + \mathbf{P}_2(\theta, \phi_a) e^{-j\psi(\theta, \phi_a)} \quad (9)$$

$$\psi(\theta, \phi_a) = \beta \frac{d}{2} \sin(\theta) \quad (10)$$

where β is the free-space propagation constant equal to $2\pi/\lambda$ with λ being the wavelength, and $\mathbf{P}_1(\theta, \phi)$ and $\mathbf{P}_2(\theta, \phi)$ are the antenna magnitudes. Due to symmetry, $\mathbf{P}_1(\theta, \phi) = \mathbf{P}_2(\theta, \phi) = \mathbf{P}(\theta, \phi)$, so

$$\mathbf{E}_\Sigma(\theta, \phi_a) = \mathbf{P}(\theta, \phi_a) [e^{j\psi(\theta, \phi_a)} + e^{-j\psi(\theta, \phi_a)}] \quad (11)$$

$$= 2 \mathbf{P}(\theta, \phi_a) \cos[\psi(\theta, \phi_a)]. \quad (12)$$

The same antennas with opposite phases are used to model the array pattern of the difference channel as [21],

$$\mathbf{E}_\Delta(\theta, \phi_a) = \mathbf{P}_1(\theta, \phi_a) e^{j\psi(\theta, \phi_a)} - \mathbf{P}_2(\theta, \phi_a) e^{-j\psi(\theta, \phi_a)} \quad (13)$$

$$= \mathbf{P}(\theta, \phi_a) [e^{j\psi(\theta, \phi_a)} - e^{-j\psi(\theta, \phi_a)}] \quad (14)$$

$$= j 2 \mathbf{P}(\theta, \phi_a) \sin[\psi(\theta, \phi_a)]. \quad (15)$$

From (1), (3), (12), and the expansion

$$\mathbf{P}(\theta, \phi_a) = P_\theta(\theta, \phi_a) \hat{\boldsymbol{\theta}} + P_\phi(\theta, \phi_a) \hat{\boldsymbol{\phi}}, \quad (16)$$

the co-polarisation sum radiation patterns in the azimuth plane are given by [20]

$$E_{\Sigma C}(\theta, \phi_a) = \mathbf{E}_\Sigma(\theta, \phi_a) \cdot \hat{\mathbf{i}}_C \quad (17)$$

$$= 2 [P_\theta(\theta, \phi_a) \hat{\boldsymbol{\theta}} + P_\phi(\theta, \phi_a) \hat{\boldsymbol{\phi}}] \cos[\psi(\theta, \phi_a)] \cdot [\sin(\phi_a) \hat{\boldsymbol{\theta}} + \cos(\phi_a) \hat{\boldsymbol{\phi}}] \quad (18)$$

$$= 2 P_\phi(\theta, \phi_a) \cos[\psi(\theta, \phi_a)]. \quad (19)$$

The same procedure applied to (15) results in the co-polarisation difference channel antenna radiation pattern

$$E_{\Delta C}(\theta, \phi_a) = j 2 P_\phi(\theta, \phi_a) \sin[\psi(\theta, \phi_a)]. \quad (20)$$

For the cross-polarisation radiation pattern in the azimuth plane, (2), (4), (12), (15), and (16) become

$$E_{\Sigma X}(\theta, \phi_a) = \mathbf{E}_\Sigma(\theta, \phi_a) \cdot \hat{\mathbf{i}}_X \quad (21)$$

$$= 2 \left[P_\theta(\theta, \phi_a) \hat{\boldsymbol{\theta}} + P_\phi(\theta, \phi_a) \hat{\boldsymbol{\phi}} \right] \cos[\psi(\theta, \phi_a)] \cdot \left[\cos(\phi_a) \hat{\boldsymbol{\theta}} - \sin(\phi_a) \hat{\boldsymbol{\phi}} \right] \quad (22)$$

$$= 2 P_\theta(\theta, \phi_a) \cos[\psi(\theta, \phi_a)] \quad (23)$$

and

$$E_{\Delta X}(\theta, \phi_a) = j 2 P_\theta(\theta, \phi_a) \sin[\psi(\theta, \phi_a)]. \quad (24)$$

The exact monopulse ratio [22] of the co-polarised components in the azimuth plane is given by

$$M_C(\theta, \phi_a) = \mathcal{Jm} \left\{ \frac{E_{\Delta C}(\theta, \phi_a)}{E_{\Sigma C}(\theta, \phi_a)} \right\} \quad (25)$$

$$= \mathcal{Jm} \left\{ \frac{j 2 P_\phi(\theta, \phi_a) \sin[\psi(\theta, \phi_a)]}{2 P_\phi(\theta, \phi_a) \cos[\psi(\theta, \phi_a)]} \right\} \quad (26)$$

$$= \tan[\psi(\theta, \phi_a)]. \quad (27)$$

The cross-polarisation pattern in the azimuth and elevation plane of the simulated antennas is approximately zero as a result of symmetry [11], therefore in these mathematical models, the cross-polarisation monopulse ratio is approximately 0/0, which is undefined.

Symmetry and the use of spherical co-ordinates mean that a similar analysis for the elevation plane where $\phi = \phi_e$ gives results with the same forms as those provided above, but with ϕ_e replacing ϕ_a . As a result, only the azimuth case will be considered below.

The main focus of this work is the evaluation of the relative magnitudes of the co- and cross-polarised patterns, so it is perhaps surprising that a result that considers the cross-polarisation components to be zero is provided. This is a result of the fact that the cross-polarisation patterns in the main planes (azimuth and elevation) are extremely small for practical antennas. As a result, the discussion now moves to the diagonal planes as there are Condon lobes in these planes, which result in significant cross-polarisation components that need to be considered.

To model cross-polarisation patterns in the diagonal plane, the condition $E_\theta(\theta, \phi_d) \approx E_\phi(\theta, \phi_d)$ must be met. To achieve this condition, constants must be introduced into (12) and (15) giving

$$E_\Sigma(\theta, \phi_d) = 2 \mathbf{P}(\theta, \phi_d) \cos[b_\Sigma \psi(\theta, \phi_d)] \quad (28)$$

$$E_\Delta(\theta, \phi_d) = j 2 \mathbf{P}(\theta, \phi_d) \sin[b_\Delta \psi(\theta, \phi_d)], \quad (29)$$

where b_Σ and b_Δ are positive real constants used to control the beamwidth of the patterns. Now the sum and difference electric fields are

$$E_{\Sigma\theta}(\theta, \phi_d) = 2 P_\theta(\theta, \phi_d) \cos[b_{\Sigma\theta} \psi(\theta, \phi_d)] \quad (30)$$

$$E_{\Sigma\phi}(\theta, \phi_d) = 2 P_\phi(\theta, \phi_d) \cos[b_{\Sigma\phi} \psi(\theta, \phi_d)] \quad (31)$$

$$E_{\Delta\theta}(\theta, \phi_d) = j 2 P_\theta(\theta, \phi_d) \sin[b_{\Delta\theta} \psi(\theta, \phi_d)] \quad (32)$$

$$E_{\Delta\phi}(\theta, \phi_d) = j 2 P_\phi(\theta, \phi_d) \sin[b_{\Delta\phi} \psi(\theta, \phi_d)]. \quad (33)$$

To maintain the condition that $E_\theta(\theta, \phi_d) \approx E_\phi(\theta, \phi_d)$ and $E_\theta(\theta, \phi_d) \neq E_\phi(\theta, \phi_d)$, then $b_{\Sigma\theta} \neq b_{\Sigma\phi}$ and $b_{\Delta\theta} \neq b_{\Delta\phi}$. Note that these results apply for both the azimuth and elevation sum and difference channels because the diagonal plane is affected by both cases.

The co-polarisation sum antenna radiation patterns in the diagonal planes can be shown to be given by

$$E_{\Sigma C}(\theta, \phi_d) = \left[E_{\Sigma\theta}(\theta, \phi_d) \hat{\boldsymbol{\theta}} + E_{\Sigma\phi}(\theta, \phi_d) \hat{\boldsymbol{\phi}} \right] \cdot \left[\sin(\phi_d) \hat{\boldsymbol{\theta}} + \cos(\phi_d) \hat{\boldsymbol{\phi}} \right] \quad (34)$$

$$= \frac{1}{\sqrt{2}} \left[E_{\Sigma\theta}(\theta, \phi_d) + E_{\Sigma\phi}(\theta, \phi_d) \right], \quad (35)$$

and substituting (30) and (31) into (35) gives

$$E_{\Sigma C}(\theta, \phi_d) = \sqrt{2} \left(P_\theta(\theta, \phi_d) \cos[b_{\Sigma\theta} \psi(\theta, \phi_d)] + P_\phi(\theta, \phi_d) \cos[b_{\Sigma\phi} \psi(\theta, \phi_d)] \right). \quad (36)$$

Following a similar procedure shows that the co-polarisation difference radiation patterns are given by

$$E_{\Delta C}(\theta, \phi_d) = j\sqrt{2} \left(P_\theta(\theta, \phi_d) \sin[b_{\Delta\theta} \psi(\theta, \phi_d)] + P_\phi(\theta, \phi_d) \sin[b_{\Delta\phi} \psi(\theta, \phi_d)] \right). \quad (37)$$

Now for the sum cross-polarisation antenna patterns,

$$E_{\Sigma X}(\theta, \phi_d) = \left[E_{\Sigma\theta}(\theta, \phi_d) \hat{\boldsymbol{\theta}} + E_{\Sigma\phi}(\theta, \phi_d) \hat{\boldsymbol{\phi}} \right] \cdot \left[\cos(\phi_d) \hat{\boldsymbol{\theta}} - \sin(\phi_d) \hat{\boldsymbol{\phi}} \right], \quad (38)$$

$$= \frac{1}{\sqrt{2}} \left[E_{\Sigma\theta}(\theta, \phi_d) - E_{\Sigma\phi}(\theta, \phi_d) \right], \quad (39)$$

and substituting (30) and (31) into (39) gives

$$E_{\Sigma X}(\theta, \phi_d) = \sqrt{2} \left(P_\theta(\theta, \phi_d) \cos[b_{\Sigma\theta} \psi(\theta, \phi_d)] - P_\phi(\theta, \phi_d) \cos[b_{\Sigma\phi} \psi(\theta, \phi_d)] \right), \quad (40)$$

with the corresponding difference cross-polarisation radiation pattern being

$$E_{\Delta X}(\theta, \phi_d) = j\sqrt{2} \left(P_\theta(\theta, \phi_d) \sin[b_{\Delta\theta} \psi(\theta, \phi_d)] - P_\phi(\theta, \phi_d) \sin[b_{\Delta\phi} \psi(\theta, \phi_d)] \right). \quad (41)$$

The co-polarisation exact monopulse ratio in the diagonal planes is

$$M_C(\theta, \phi_d) = \mathcal{Jm} \left\{ \frac{E_{\Delta C}(\theta, \phi_d)}{E_{\Sigma C}(\theta, \phi_d)} \right\} \quad (42)$$

$$= \frac{\sin [b_{\Delta\theta} \psi (\theta, \phi_d)] + \sin [b_{\Delta\phi} \psi (\theta, \phi_d)]}{\cos [b_{\Sigma\theta} \psi (\theta, \phi_d)] + \cos [b_{\Sigma\phi} \psi (\theta, \phi_d)]}, \quad (43)$$

and the cross-polarisation exact monopulse ratio is

$$M_X (\theta, \phi_d) = \frac{\sin [b_{\Delta\theta} \psi (\theta, \phi_d)] - \sin [b_{\Delta\phi} \psi (\theta, \phi_d)]}{\cos [b_{\Sigma\theta} \psi (\theta, \phi_d)] - \cos [b_{\Sigma\phi} \psi (\theta, \phi_d)]}. \quad (44)$$

The co- and cross-polarisation monopulse ratios in (43) and (44) result in the expected polarisation component patterns at the diagonal planes.

B. Technique 2

This technique differs from Technique 1 in that it does not directly use Ludwig's polarisation definitions. The co- and cross-polarisation components for an axially-symmetrical parabolic reflector antenna are modelled [21], but only the sum patterns. The sum channel antenna co- and cross-polarisation component radiation patterns are given by [21]

$$E_{\Sigma C} (\theta, \phi) = AP_{\Sigma C} (\theta, \phi) f_C (\theta, \phi) \quad (45)$$

$$E_{\Sigma X} (\theta, \phi) = AP_{\Sigma X} (\theta, \phi) f_X (\theta, \phi), \quad (46)$$

respectively, where $AP_{\Sigma C} (\theta, \phi)$ and $AP_{\Sigma X} (\theta, \phi)$ are array patterns and in this work, they are modelled differently from [21] to suit the goals of this work. The functions $f_C (\theta, \phi)$ and $f_X (\theta, \phi)$ are used to convert the sum-channel array pattern function to co- and cross-polarisation components and are given by [21]

$$f_C (\theta, \phi) = \left[\cos (\theta) \cos^2 (\phi) + \sin^2 (\phi) \right] \quad (47)$$

$$f_X (\theta, \phi) = \left[[\cos (\theta) - 1] \sin (\phi) \cos (\phi) \right]. \quad (48)$$

The co- and cross-polarisation sum channel array patterns are modelled as

$$AP_{\Sigma C} (\theta, \phi) = \cos (m_{\Sigma C} \theta) P (m_{\Sigma C} \theta) \quad (49)$$

$$AP_{\Sigma X} (\theta, \phi) = \cos (m_{\Sigma X} \theta) P (m_{\Sigma X} \theta), \quad (50)$$

respectively, where $m_{\Sigma C}$ and $m_{\Sigma X}$ are used to control the beamwidth of the patterns, and the element pattern, $P (\theta)$, is assumed to be a sinc function in this work, though other element patterns can be used. The array patterns are products of the relevant array factors and element patterns [21].

Equations (47) and (48) are only used to convert the sum-channel array patterns to co- and cross-polarisation components across all the planes. This can be seen from the way (47) and (48) depend on both θ and ϕ , while the array patterns in (49) and (50) depend only on θ which is the off-boresight angle.

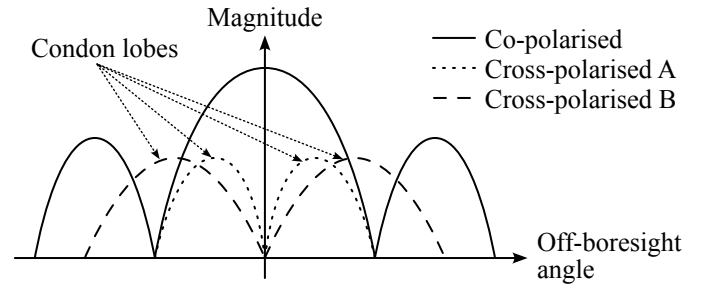


Fig. 2. The effect of the co- and cross-polarised antenna-pattern models having equal and unequal beamwidths is shown by patterns A and B, respectively.

In Technique 1, the sum co- and cross-polarisation patterns are determined from the same array pattern function. But in this technique, the beamwidth of the co-polarised array pattern in (49), is not equal to that of the cross-polarised array pattern in (50). If these two patterns were equal, the Condon lobes would be located where the cross-polarised A pattern is located in Fig. 2, which is undesirable because the Condon lobes of practical antennas are not within the co-polarised sum-channel pattern [1], [7], [21], [23]. With reference to the antennas analysed in this work, the Condon lobes must be located where the cross-polarised pattern B is located in Fig. 2.

The above results focus on the sum-channel patterns [21], not the difference patterns. For (45) and (46) to be useful for cross-polarisation analysis, the difference-channel patterns must also be modelled. To derive the azimuth difference patterns, the knowledge that the co-polarisation in the azimuth difference channel pattern has a null along the elevation axis and its cross-polarisation component has a null along the azimuth axis and vice-versa for the elevation difference channel is applied [23]. The co-polarisation component for the azimuth difference channel is taken as the cross-polarisation component for the elevation difference channel but with reduced amplitude and vice-versa.

The azimuth co- and cross-polarisation difference-channel antenna radiation patterns are modelled as

$$E_{a\Delta C} (\theta, \phi) = AP_{\Delta} (\theta, \phi) \cos (\phi) \quad (51)$$

$$E_{a\Delta X} (\theta, \phi) = k_{aX} AP_{\Delta} (\theta, \phi) \sin (\phi), \quad (52)$$

respectively, where k_{aX} is the constant used to scale the magnitude of the cross-polarisation component. It must be noted that the array patterns in (51) and (52) are multiplied by $\cos (\phi)$ and $\sin (\phi)$ respectively, and these sinusoidal functions depend only on ϕ . The $\cos (\phi)$ factor is used to convert the difference channel array pattern to a co-polarisation pattern across all ϕ planes, while the $\sin (\phi)$ factor converts it to a cross-polarisation pattern

across all ϕ planes.

The difference-channel array pattern $AP_{\Delta}(\theta, \phi)$ is modelled as

$$AP_{\Delta}(\theta, \phi) = \sin(m_{\Delta}\theta) P(m_{\Delta}\theta) \quad (53)$$

where m_{Δ} is a positive real value used to control the radiation pattern beamwidth. The array pattern is independent of the ϕ plane angle, which is why it must be multiplied by a function that depends on ϕ .

The antenna radiation pattern co- and cross-polarisation components in the elevation difference channel are modelled as

$$E_{e\Delta C}(\theta, \phi) = k_{eC} E_{a\Delta X}(\theta, \phi) \quad (54)$$

$$E_{e\Delta X}(\theta, \phi) = k_{eX} E_{a\Delta C}(\theta, \phi), \quad (55)$$

respectively, where k_{eC} and k_{eX} are magnitude scaling constants used to scale the radiation patterns. The azimuth co- and cross-polarisation monopulse ratios are

$$M_{aC}(\theta, \phi) = \frac{E_{a\Delta C}(\theta, \phi)}{E_{\Sigma C}(\theta, \phi)} \quad (56)$$

$$= \frac{AP_{\Delta}(\theta, \phi)}{AP_{\Sigma C}(\theta, \phi)} \times \frac{\cos(\phi)}{\cos(\theta)\cos^2(\phi) + \sin^2(\phi)} \quad (57)$$

$$M_{aX}(\theta, \phi) = \frac{E_{a\Delta X}(\theta, \phi)}{E_{\Sigma X}(\theta, \phi)} \quad (58)$$

$$= \frac{k_{aX} AP_{\Delta}(\theta, \phi)}{AP_{\Sigma X}(\theta, \phi)} \times \frac{\sin(\phi)}{[\cos(\theta) - 1] \sin(\phi) \cos(\phi)}, \quad (59)$$

respectively. To determine the elevation monopulse ratio, (54) and (55) should be used as the numerators of (56) and (58), respectively.

C. Theoretical Modelling Simulation Results

To determine the induced angular error [22],

$$\theta_{\text{ampl}} = \arcsin \left[\frac{2}{\beta d} \arctan(\Re\{M_s\}) \right] \quad (60)$$

$$\theta_{\text{phase}} = \arcsin \left[\frac{2}{\beta d} \arctan(\Im\{M_s\}) \right] \quad (61)$$

are used to determine the off-boresight angles, θ_{ampl} and θ_{phase} , for amplitude- and phase-comparison monopulse, respectively.

The monopulse ratio is

$$M_s(\theta, \phi) = \frac{E_{\Delta}(\theta, \phi)}{E_{\Sigma}(\theta, \phi)} \quad (62)$$

with

$$E_{\Delta}(\theta, \phi) = E_{\Delta C}^{\text{tr}}(\theta, \phi) + E_{\Delta X}^{\text{jr}}(\theta, \phi) \quad (63)$$

$$E_{\Sigma}(\theta, \phi) = E_{\Sigma C}^{\text{tr}}(\theta, \phi) + E_{\Sigma X}^{\text{jr}}(\theta, \phi) \quad (64)$$

giving

$$M_s(\theta, \phi) = \frac{E_{\Delta C}^{\text{tr}}(\theta, \phi) + E_{\Delta X}^{\text{jr}}(\theta, \phi)}{E_{\Sigma C}^{\text{tr}}(\theta, \phi) + E_{\Sigma X}^{\text{jr}}(\theta, \phi)}, \quad (65)$$

where $E_{\Sigma X}^{\text{jr}}(\theta, \phi)$ and $E_{\Sigma C}^{\text{tr}}(\theta, \phi)$ are the sum-channel returns of the cross-polarisation jammer and the target, respectively, and $E_{\Delta X}^{\text{jr}}(\theta, \phi)$ and $E_{\Delta C}^{\text{tr}}(\theta, \phi)$ are the difference-channel returns of the cross-polarisation jammer and the target, respectively.

Equation (65) is used show the effect of increasing the cross-polarisation signal power while the co-polarisation signal power is constant because the JSR is determined by the ratio of the cross-polarisation signal to the co-polarisation signal. To determine the angular error, the co-polarisation signal component is kept constant while the cross-polarisation signal component power is increased.

The mathematical modelling results are shown in Figs 3 and 4. Even though only the radiation patterns and monopulse ratios for Technique 1 are presented, the angular error results are generated from both techniques.

To generate the results for both techniques at the $\phi = 45^\circ$ diagonal plane, the $E_{\theta}(\theta, \phi_d)$ and $E_{\phi}(\theta, \phi_d)$ of the designed antennas were analysed and showed similar behaviour with $E_{\theta}(\theta, \phi_d) \approx E_{\phi}(\theta, \phi_d)$. The $E_{\theta}(\theta, \phi_d)$ and $E_{\phi}(\theta, \phi_d)$ magnitudes for both sum and difference patterns were averaged at the main lobes for a monopulse wire-grid antenna [24, Fig. 9] that will be considered in more detail in Section IV.

The values averaged from the wire-grid antenna are used as constants for Technique 1 and are $b_{\Sigma\theta} = 4.6180$, $b_{\Sigma\phi} = 5.2963$, $b_{\Delta\theta} = 2.8643$, and $b_{\Delta\phi} = 2.4919$. The radiation patterns and monopulse ratio generated from Technique 1 are shown in Figs 3(a) and 3(b).

The values of the constants needed by Technique 2 are $m_{\Sigma C} = 4$, $m_{\Sigma X} = 2$, and $m_{\Delta} = 5$. It can be noted that the constants in Technique 1 have greater precision than the constants in Technique 2. This is not because Technique 1 requires highly accurate values while Technique 2 does not; it is because the constants in Technique 1 were averaged from radiation pattern magnitudes of the wire-grid antenna, while the constants in Technique 2 were manually tuned to match the antenna radiation patterns.

Technique 2 has only three constants that can be tuned according to the desired radiation pattern shape or size, or the location of the Condon lobes as explained

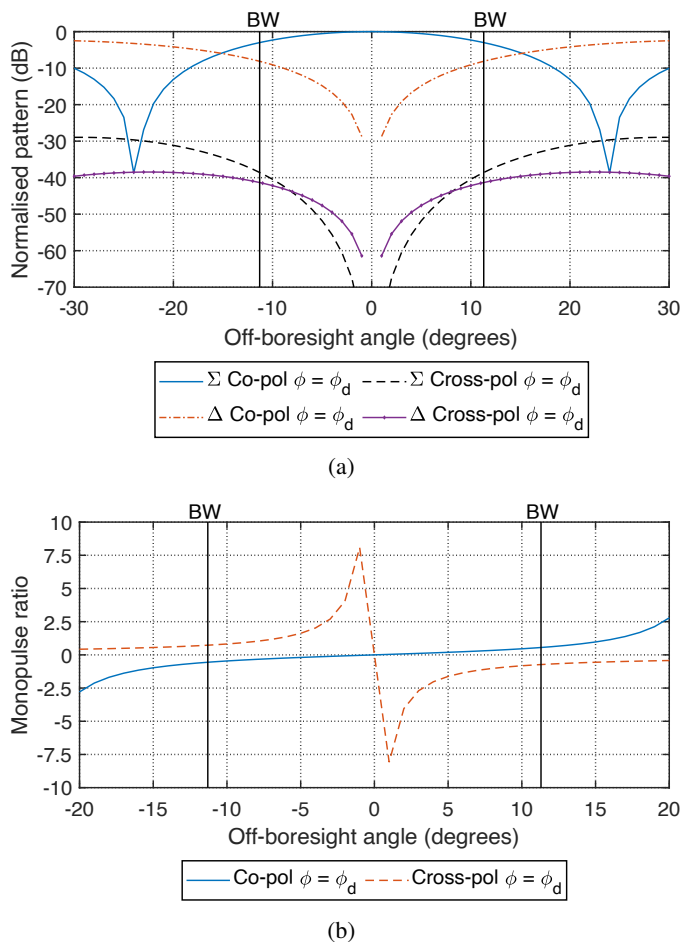


Fig. 3. The results from Technique 1 in the $\phi_d = 45^\circ$ diagonal plane showing (a) the radiation patterns, and (b), the monopulse ratios. BW denotes the 3-dB sum-channel beamwidth of the antenna.

in Section II-B. In this work, these constant values that control the beamwidth of the radiation patterns were tuned so that the Condon lobes follow case B in Fig. 2 because this is the location of Condon lobes in monopulse antennas [1], [7], [21], [23].

Fig. 3(a) shows that the co-polarisation sum pattern has a peak lobe on boresight while the cross-polarisation sum pattern has a null on boresight with off-boresight peaks (Condon lobes). The co- and cross-polarisation difference patterns have nulls on boresight. Fig. 3(b) shows the monopulse ratios, and it is seen that the co-polarisation monopulse ratio has a smooth transition on boresight while cross-polarisation monopulse ratio shows distortion. The radiation patterns and monopulse ratios of Technique 1 show that the mathematical derivation and the use of the $b_{\Sigma\theta}$, $b_{\Sigma\phi}$, $b_{\Delta\theta}$, and $b_{\Delta\phi}$ values from the wire-grid antenna results in radiation patterns and monopulse ratios that are comparable to those seen in the simulated antennas in Figs 6(a) and 6(b) in Section III, respectively [23].

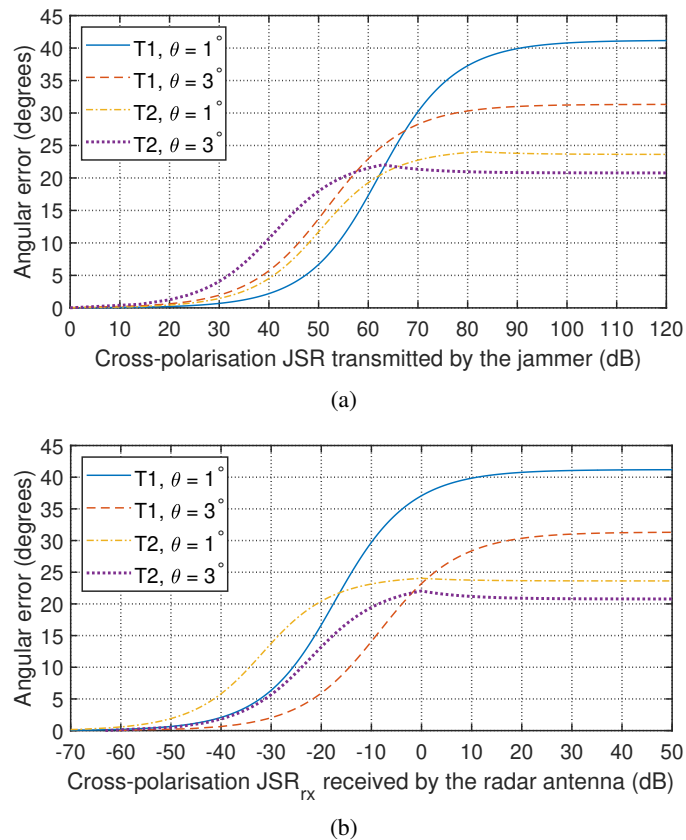


Fig. 4. The induced angular error results from the two techniques in the $\phi_d = 45^\circ$ diagonal plane showing the angular error versus the JSR (a) at the jammer and (b) at the input to the monopulse comparator (JSR_{rx}). T1 and T2 denote Techniques 1 and 2, respectively.

During target tracking, the radar uses the main lobe located on boresight, but if the cross-polarisation jammer has high JSR, the tracking radar will be forced to track using one of the Condon lobes. The angular error induced as the JSR is increased as shown in Fig. 4 for targets positioned at $\theta = 1^\circ$ and 3° off-boresight. The perfect symmetry of the simulations means that there is no cross-polarisation component at $\theta = 0^\circ$ [11], so off-boresight angles are required to obtain results.

Fig. 4 shows two figures plotted with the same angular error against two different JSR values. Fig. 4(a) shows the angular error against the JSR at the jammer, which is the ratio of the jammer power of the cross-polarisation signal to the co-polarisation signal target return power – the JSR definition normally applied to cross-polarisation jamming. The radiation patterns in Fig. 3(a) have a JSR of 0 dB.

The antenna gains of the co- and cross-polarisation components are not equal and vary with angle. At $\phi = 1^\circ$, the cross-polarisation antenna gain is approximately 70 dB less than the co-polarisation antenna gain. The ratio of cross-polarisation signal magnitude

to co-polarisation signal magnitudes received by the monopulse processor (i.e. after being subjected to the different antenna gains of the co- and cross-polarisation components of the monopulse antenna) is JSR_{rx} , and it is the JSR seen in Fig. 4(b).

The induced angular error in Fig. 4(a) increases more rapidly from $JSR \approx 20$ dB. For Technique 1 at $\theta = 1^\circ$ and $\theta = 3^\circ$, the angular error increases more slowly as the JSR increases, and reaches a constant angular error at $JSR \approx 60$ dB and 80 dB, respectively. For Technique 2 at $\theta = 1^\circ$ and $\theta = 3^\circ$, the angular error stops increasing and reaches a constant angular error at $JSR = 82$ dB and $JSR = 64$ dB, respectively. The angular error stops increasing and becomes constant because this is the point where the $JSR_{rx} \approx 0$ dB as seen in Fig. 4(b). These are the points where the JSR starts exceeding the polarisation purity of the antenna, and as a result, the cross-polarised signal magnitude at the monopulse processor starts exceeding the co-polarised signal magnitude at the monopulse processor.

Looking at the off-boresight target angles $\theta = 1^\circ$ and $\theta = 3^\circ$ in Fig. 4, both techniques show that the angular error decreases as the target return moves away from boresight, which is expected because tracking accuracy decreases as the target moves away from the linear section of the monopulse ratio near boresight ($\theta = 0^\circ$). Even though $\theta = 3^\circ$ is still within the beamwidth and not far away from the linear section of the monopulse ratio in Fig. 3(b), it still shows that the difference between a linear fit to the monopulse ratio near boresight and the true monopulse ratio increases when moving away from boresight towards the 3 dB beamwidth edge.

The two techniques produce different angular errors, which is primarily as a result of different polarisation purity values. The polarisation purities at $\theta = 1^\circ$ and $\theta = 3^\circ$ are 79.53 dB and 60.46 dB, respectively, for Technique 1, and 82.34 dB and 63.09 dB, respectively, for Technique 2. It is this difference that leads to Technique 2 producing lower angular errors than Technique 1 for the example considered here.

III. ANTENNA ANALYSIS RESULTS AND MEASUREMENTS

The five antennas shown in Fig. 5 were designed and analysed using Altair Feko Solver 2021.1-5769. These antennas were chosen because they represent planar array antennas and a variety of parabolic reflector antennas.

All the antennas considered operate at 10 GHz, unless otherwise noted. However, the results provided are applicable at all frequencies due to the well-known scaling property of antennas [25].

TABLE I
THE PARAMETERS OF THE X- AND C-BAND WIRE-GRID ANTENNAS SHOWN IN FIG. 5(A) [26]

Parameters	X-band (mm)	C-band (mm)
Substrate height	1.4990	0.8130
Horizontal gap	8.2550	23.4800
Vertical gap	2.5654	11.7800
w1	5.3086	12.3800
w2	2.2606	9.2640
w3	0.7366	6.5680
w4	2.8194	3.0430
w5	1.1684	2.8830
w6	0.2540	8.5440
w7	1.9304	3.9670
w8	1.4732	5.1710
w9	0.3556	0.6883
w10	1.0414	0.6941
w11	0.4064	3.1140
w12	0.6096	0.6947
w13	0.3302	0.6834
w	0.2540	0.7403

The wire-grid antenna shown in Fig. 5(a) is representative of planar antennas, and its parameters are tabulated in Table I. The four-horn monopulse antenna shown in Fig. 5(b) is used as a feed for the parabolic antennas and is also analysed separately to represent horn-based monopulse antennas. The parabolic reflector antennas are represented by three reflector antennas, a parabolic reflector antenna shown in Fig. 5(c), and two Cassegrain parabolic antennas shown in Figs 5(d) and 5(e). The two Cassegrain antennas are designed differently, and their four-horn feeds are at different locations as shown in Figs 5(d) and 5(e). Not all categories and types of antennas can be included in this work, but the antennas considered represent monopulse antennas that have cross-polarisation Condon lobes in their diagonal planes.

The first antenna is the wire-grid phase-comparison monopulse antenna developed by Conti *et al.* [24, Fig. 9], and is shown in Fig. 5(a). The substrate used has a dielectric constant of 2.2 and a height of 0.05 wavelength. This antenna has a sidelobe level (SLL) of below -20 dB and a gain of 21.5 dBi as a result of using the Taylor distribution tapering method that resulted in a taper loss of 0.5 dB [23]. The wire-grid antenna was selected as the antenna to be manufactured, so it was re-designed at 5.5 GHz frequency using RO4003C substrate with a dielectric constant of 3.38 and thickness of 0.813 mm.

The second antenna is the four-horn phase-comparison monopulse antenna shown in Fig. 5(b). This antenna

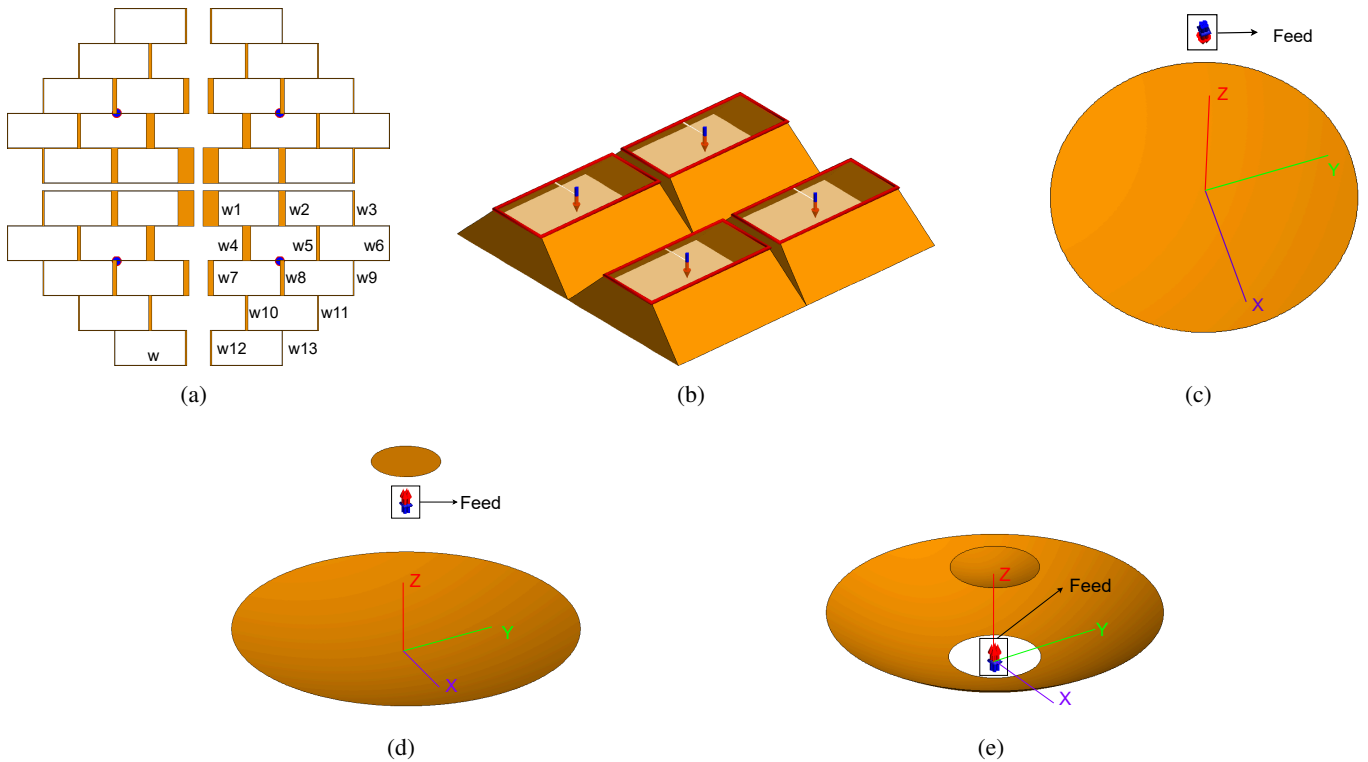


Fig. 5. The geometry of the analysed monopulse antennas, namely (a) a wire-grid antenna, (b) a four-horn antenna that is also the feed of the reflector antennas, (c) a Hannan parabolic antenna, (d) a Cassegrain antenna, and (e) a Hannan Cassegrain antenna [23], [26].

comprises four horns with WR90 waveguide feeds of $22.86 \text{ mm} \times 10.16 \text{ mm}$, and an aperture width and height of 22.86 mm , where the wider walls of the horn antennas being at an angle of 45° to give a horn length of 6.35 mm [23]. This antenna configuration was also used as the feed of the reflector antennas described below.

The third antenna is the amplitude-comparison monopulse shown in Fig. 5(c) and is based on Hannan's guidelines for parabolic reflectors in monopulse antennas [27, Fig. 5]

$$\frac{aA}{2\lambda F} = 0.69 \quad \text{and} \quad \frac{bB}{2\lambda F} = 0.71 \quad (66)$$

where a and b are the width and height of the feed horns, respectively, A and B are the dimensions of the reflector, and F is the focal length. The radius of the reflector was selected to be 1 m ($A = B = 2 \text{ m}$), and the horn apertures were $a = 25.00 \text{ mm}$ by $b = 24.30 \text{ mm}$, which gives a focal length of $F = 2.35 \text{ m}$.

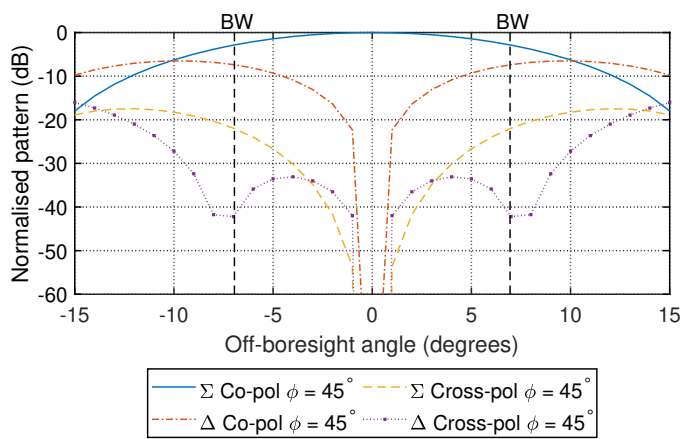
The fourth antenna is the amplitude-comparison Cassegrain monopulse antenna shown in Fig. 5(d). Its parabolic reflector focal length, radius, and segment length are 1.5 m and 1.0 m , respectively, and its hyperbolic reflector focal length and radius are 266.7 mm and 200 mm , respectively.

The fifth antenna is shown in Fig. 5(e) and is an

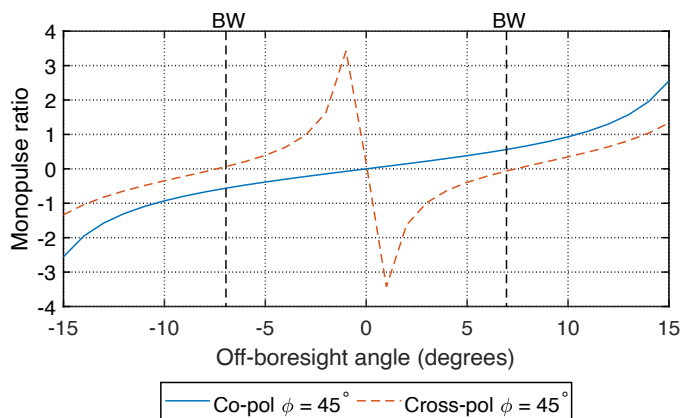
amplitude-comparison Hannan Cassegrain monopulse antenna. Its parabolic reflector focal length and radius are 0.78 m and 1.0 m , respectively. Its hyperbolic reflector radius and magnification are 0.2657 m and 0.1958 m , respectively, and its hyperbolic reflector is placed 0.59 m from the parabolic reflector.

The Feko simulation results of the monopulse wire-grid antenna in Fig. 6 show that the co-polarisation sum pattern has a peak on boresight while its cross-polarisation patterns have nulls on boresight and Condon lobes off boresight. Both polarisation components of the difference patterns have a null on boresight. The cross-polarisation monopulse ratio shows distortion on boresight. The distortion of the cross-polarisation monopulse ratio on boresight is because both the cross-polarised difference pattern and the cross-polarised sum pattern have nulls at boresight which causes this distortion, unlike the co-polarised monopulse ratio where only the difference channel has a null at boresight.

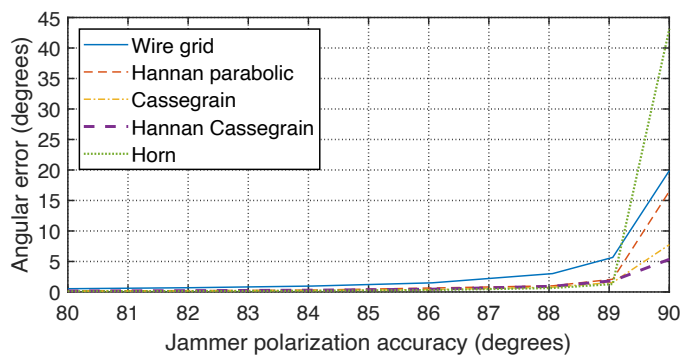
Fig. 7 shows the angular error induced in the monopulse radar by a cross-polarised jamming signal. These angular results show comparable behaviour to those seen in the mathematical models in Fig. 4, in that the angular error stops increasing and becomes constant when the JSR_{rx} is equal to or greater than 0 dB , which is when the JSR is higher than the antenna's polarisation purity.



(a)



(b)

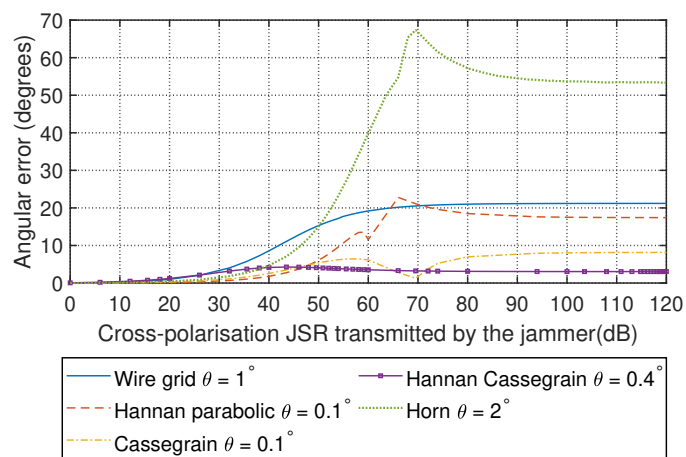


(c)

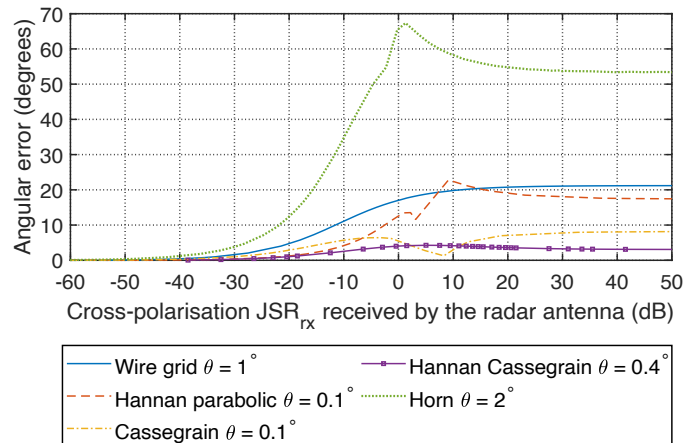
Fig. 6. The simulated results of the antennas in the diagonal plane show (a) the wire-grid antenna radiation patterns, (b) the wire-grid antenna monopulse ratios, (c) the effect of jammer polarization accuracy on the induced angular error in each antenna. BW denotes the 3-dB sum-channel beamwidth of the antenna.

The angular error is approximately 0° from 0 dB to 20 dB JSR, but increases rapidly at higher JSR values. This occurs at a JSR of $JSR = 55$ dB for the wire-grid antenna, 70 dB for the four-horn antenna, 60 dB for the Hannan parabolic antenna, 60 dB for the Cassegrain antenna, and 40 dB for the Hannan Cassegrain antenna.

The ability of the jammer to accurately reproduce the



(a)



(b)

Fig. 7. The simulated results due to the signal in the diagonal plane showing the induced angular error versus the cross-polarisation JSR (a) at the jammer and (b) at the input to the monopulse comparator (JSR_{rx}).

polarisation of the signal being jammed is extremely important in cross-polarisation jamming [1]. The induced angular errors resulting from the polarisation angle errors are shown Fig. 6(c), where 0° corresponds to perfect co-polarisation, moving towards perfect cross-polarisation at 90° . Over a polarisation angles of 0° to 80° , the induced angular error is approximately 0° , so only data from 80° to 90° is included. At the perfect cross-polarisation angle of 90° , the jammer polarization is accurate, hence the jammer induces a high angular error into the radar being jammed. However, the jammer loses an average of approximately 86%, 90%, and 95% of the induced angular error across all the antennas with polarisation errors of only 1° , 2° , and 4° , respectively.

The results for the manufactured wire-grid antenna are shown in Fig. 8, where it can be seen that the co-polarisation sum pattern has a peak on boresight and its cross-polarisation sum pattern has a null on boresight and

peaks off boresight (Condon lobes). Both the polarisation components of the difference pattern have nulls on boresight. The cross-polarisation monopulse ratio has a distorted slope on boresight as expected.

The effect of the polarisation accuracy of the jammer at various frequency points is shown in Fig. 8(c), with 0° and 90° being the perfect co- and cross-polarisation angles, respectively. Only data from 80° to 90° are shown, with the antenna showing that if the jammer is off by approximately 2° and 5° , it loses an average of approximately 62% and 85% of its induced angular error, respectively. The effect of jammer polarisation accuracy seen in Figs 6(c) and 8(c) is aligned with cross-polarisation jammer polarisation accuracy effects noted elsewhere [1, Fig. 207], thereby providing some measure of validation of the results.

IV. COMPARISON AND DISCUSSION

The co-polarisation sum patterns generated from the mathematical models and those generated from the designed antennas in Feko have peaks on boresight, and their co- and cross-polarisation difference-channel patterns have nulls on boresight, while their cross-polarisation sum channel patterns have Condon lobes off boresight, as expected. The measured cross-polarisation patterns in Fig. 8(a) have nulls and Condon lobes, but they are not as well defined as in the theoretical and simulated results in Figs 3(a) and 6(a), respectively. This is because theoretical modelling and Feko simulations are ideal while the measured system is not. Additionally, cross-polarisation measurements are complicated by low signal levels and the need for accurate misalignment, with even small misalignments potentially causing large errors [18].

The polarisation purity of the antenna plays a crucial role during cross-polarisation jamming, and antennas with high polarisation purity require the jammer to have higher JSR than antennas with low polarisation purity. Between the Hannan parabolic reflector and the wire-grid antenna in Fig. 7, a higher angular error is induced into the wire-grid antenna than the Hannan parabolic reflector antenna because the Hannan parabolic reflector has higher polarisation purity than the wire-grid antenna [23].

In the parabolic reflector antennas, the Condon lobe size is controlled by the focal-length-to diameter ratio (F/D) ratio, and increasing the F/D ratio reduces the Condon lobes and increases the polarisation purity [8], [9], [10]. From the perspective of electronic protection (EP) against cross-polarisation jamming, parabolic antennas should thus be designed to have F/D ratios that are as large as possible to increase polarisation purity.

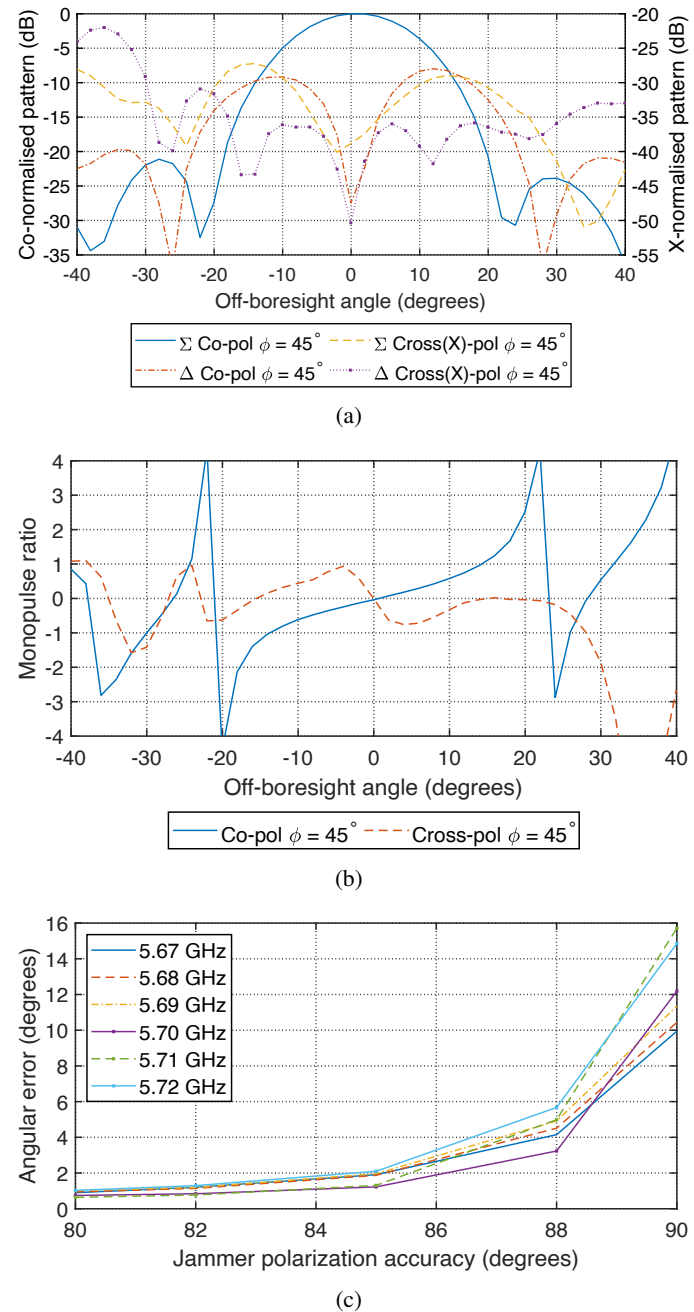


Fig. 8. The measured results for the wire-grid antenna in the diagonal plane showing (a) the radiation patterns at 5.67 GHz, (b) the monopulse ratios at 5.67 GHz, and (c) the effects of polarisation accuracy on the angular error.

The induced angular error results of the two techniques in the theoretical mathematical results are different in magnitude because of their difference in polarisation purity. As noted at the end of Section II-C, this explains why the angular error is higher in Technique 1 than in Technique 2. But both techniques show angular errors with a similar pattern to that in the Feko simulation results. The constants used in Technique 1 to control the radiation pattern beamwidth were calculated from the

wire-grid antenna simulated in Feko, and it is seen that the induced angular error curve for Technique 1 in Fig. 4 shows a similar pattern to the induced angular error curve in Fig. 7 for the wire-grid antenna. The other antennas in Fig. 7 show the induced angular error curve pattern similar to the curve pattern for Technique 2 in Fig. 4.

V. CONCLUSION

Mathematical models of cross-polarisation jamming were derived, and their validity was demonstrated by comparing the resulting antenna patterns to those seen in simulated and measured antennas. In both the simulated and mathematical results, the induced angular error increases at an increasing rate when JSR is greater than 20 dB, which is in line with the widely-noted claim that the JSR must be between 20 dB and 40 dB for a cross-eye jammer to induce an angular error in a radar [5], [12].

The cross-polarisation jammer depends strongly on its ability to correctly detect the polarisation angles of the radar signal and to re-transmit the signal with accurate polarisation. The polarisation accuracy results obtained agree with reported results indicating that a cross-polarisation jammer must have polarisation accuracy within 1° to 5° to be effective [4], [5], [12].

REFERENCES

- [1] L. B. Van Brunt, *Applied ECM*. Dunn Loring, VA: EW Engineering, 1978.
- [2] D. L. Adamy, *EW 101: A First Course in Electronic Warfare*. Norwood, MA: Artech House, 2001.
- [3] D. L. Adamy, *EW 104: Electronic Warfare Against a New Generation of Threats*. Norwood, MA: Artech House, 2015.
- [4] F. Neri, *Introduction to Electronic Defense Systems*, 3rd ed. Boston: Artech House, 2018.
- [5] D. C. Schleher, *Introduction to Electronic Warfare*. Norwood, MA: Artech House, 1986.
- [6] R. N. Lothes, M. B. Szymanski, and R. G. Wiley, *Radar Vulnerability to Jamming*. Norwood, MA: Artech House, 1990.
- [7] D. C. Schleher, *Electronic Warfare in the Information Age*. Norwood, MA: Artech House, 1999.
- [8] D. G. Bodnar, "Cross-polarized characteristics of monopulse difference patterns," in *Antennas Propag. Soc. Int. Symp.*, Quebec, Canada, 2–6 Jun. 1980, pp. 477–480.
- [9] S. I. Ghobrial, "Co-polar and cross-polar diffraction images in the focal plane of paraboloidal reflectors: A comparison between linear and circular polarization," *IEEE Trans. Antennas Propag.*, vol. 24, no. 4, pp. 418–424, Jul. 1976.
- [10] E. M. T. Jones, "Paraboloid reflector and hyperboloid lens antennas," *IRE Trans. Antennas Propag.*, vol. 2, no. 3, pp. 119–127, Jul. 1954.
- [11] S. I. Ghobrial, "Axial cross polarization in reflector antennas with surface imperfections," *IEEE Trans. Antennas Propag.*, vol. 28, no. 5, pp. 610–616, Sep. 1980.
- [12] E. J. Chrzanowski, *Active Radar Electronic Countermeasures*. Norwood, MA: Artech House, 1990.
- [13] A. Golden, *Radar Electronic Warfare*. Washington, DC: American Institute of Aeronautics and Astronautics (AIAA), 1987.
- [14] H. Han, X. Xu, H. Wang, and H. Dai, "Analysis of cross-polarization jamming for phase comparison monopulse radars," in *Int. Conf. Electron. Inf. Commun. Technol. (ICEICT)*, Harbin, China, Jan. 2019, pp. 404–407.
- [15] W. P. du Plessis, "Modelling monopulse antenna patterns," in *Saudi Int. Electron. Commun. Photon. Conf. (SIECPC)*, Riyadh, Saudi Arabia, 27–30 Apr. 2013, pp. 1–5.
- [16] I. Kalinbacak, M. Pehlivan, and K. Yegin, "Cross polarization monopulse jammer located on UAV," in *Proceedings of 8th International Conference on Recent Advances in Space Technologies, RAST*, Istanbul, Turkey, Aug. 2017, pp. 337–341.
- [17] H. Dai, J. Yin, Z. Liu, H. Wang, J. Wang, and L. Wang, "Cross polarization jamming and ECM performance of polarimetric fusion monopulse radars," in *Int. Conf. Comput. Eng. Netw.*, Singapore, 16–18 Oct. 2020, pp. 612–622.
- [18] A. C. Ludwig, "The definition of cross polarization," *IEEE Trans. Antennas Propag.*, vol. 21, no. 1, pp. 116–119, Jan. 1973.
- [19] W. P. du Plessis, "A comprehensive investigation of retro-directive cross-eye jamming," Ph.D. dissertation, University of Pretoria, Pretoria, RSA, 2010.
- [20] W. L. Stutzman, *Polarization in Electromagnetic Systems*, 2nd ed. Norwood, MA: Artech House, 2018.
- [21] W. L. Stutzman and G. A. Thiele, *Antenna Theory and Design*, 3rd ed. Hoboken, NJ: Wiley, 2013.
- [22] S. M. Sherman and D. K. Barton, *Monopulse Principles and Techniques*, 2nd ed. Boston: Artech House, 2011.
- [23] W. P. du Plessis and K. Mosoma, "Initial results for cross-polarisation jamming of monopulse radar," in *Int. Conf. Electromagn. Adv. Appl. (ICEAA)*, Cape Town, South Africa, 5–9 Sep. 2022, pp. 258–263.
- [24] R. Conti, J. Toth, T. Dowling, and J. Weiss, "The wire grid microstrip antenna," *IEEE Trans. Antennas Propag.*, vol. 29, no. 1, pp. 157–166, Jan. 1981.
- [25] C. A. Balanis, *Antenna Theory: Analysis and Design*, 4th ed. Hoboken, NJ: Wiley, 2016.
- [26] K. Mosoma, "Monopulse radar analysis for cross-polarisation jamming," M. Eng. Dissertation, University of Pretoria, Pretoria, RSA, 2024.
- [27] P. Hannan, "Optimum feeds for all three modes of a monopulse antenna II: Practice," *IRE Trans. Antennas Propag.*, vol. 9, no. 5, pp. 454–461, Sep. 1961.



Khahliso Mosoma received the B.Eng. (Electronic), B.Eng.(Hons) (Electronic), and M.Eng. (Electronic) degrees from the University of Pretoria in 2020, 2021, and 2024 respectively. He is currently a radar signal analyst at the Council for Scientific and Industrial Research (CSIR). His interests are cross-polarisation jamming, antenna design, and radar signal processing.



Warren P. du Plessis (M'00, SM'10) received the B.Eng. (Electronic), M.Eng. (Electronic), and Ph.D. (Engineering) degrees from the University of Pretoria in 1998, 2003, and 2010, respectively, winning numerous academic awards including the prestigious Vice-Chancellor and Principal's Medal. He is an Associate Editor of the IEEE Transactions on

Aerospace and Electronic Systems.

He spent two years as a lecturer at the University of Pretoria, and then joined Grintek Antennas as a design engineer for almost four years, followed by six years at the Council for Scientific and Industrial Research (CSIR). He is currently a Professor at the University of Pretoria, and his primary research interests are cross-eye jamming and thinned antenna arrays.